

Mechanisms of Guinier–Preston zone hardening in the athermal limit

C.V. Singh, D.H. Warner*

School of Civil and Environmental Engineering, Cornell University, Ithaca, NY 14853, USA

Received 21 April 2010; received in revised form 21 June 2010; accepted 25 June 2010

Abstract

The interaction of dislocations with Guinier–Preston (GP) zones is a process that contributes to the yield strength of many underaged precipitate-strengthened alloys. Here we use atomistic modeling to investigate this process in an Al–Cu alloy using a newly developed interatomic potential. The study focuses on edge dislocation interactions in the athermal limit. The critical shear stress and the mechanism by which dislocations overcome GP zones is found to vary significantly depending upon GP zone size, orientation and offset from the dislocation glide plane. Dislocation cutting, looping, leading partial cutting with trailing partial looping, diffusionless climb and defect nucleation at the dislocation–GP zone contact point are all observed. In the majority of cases dislocation looping is the controlling mechanism, challenging the applicability of traditional continuum dislocation cutting models to the underaged Al–Cu system at 0 K. © 2010 Acta Materialia Inc. Published by Elsevier Ltd. All rights reserved.

Keywords: Al alloy; Guinier–Preston zones; Precipitation hardening; Atomistic simulation; Dislocation–obstacle interaction

1. Introduction

A large class of commercial alloys derive their strength from precipitation hardening. Precipitates inhibit dislocation glide and thereby act to increase flow stress. For many alloys, e.g. Al–Cu, Al–Zn, Al–Cu–Zn, Cu–Be, Fe–Mo, Al–Ag and Al–Mg–Si, the precipitation process begins with the formation of nanometer-sized coherent metastable precipitates known as Guinier–Preston (GP) zones [1,2]. While the size of GP zones makes them invisible to optical microscopy, they are responsible for the increase in strength observed during the early stages of aging. As such, GP zones represent a key component of the precipitate aging processes.

GP zones, being the first precipitates to form during the aging process, are typically associated with an underaged alloy. They provide hardening by impeding dislocation glide. A variety of mechanisms for GP zone dislocation interaction are proposed in the vast literature on the subject. Elastically, misfit stresses associated with the differ-

ence in lattice constant between the GP zone and the matrix [3,4] and differences in elastic modulus between the GP zone and the matrix [5,6] have been pointed to as mechanisms for GP zone strengthening. Chemically, differences in stacking fault energy between the precipitate and the matrix [7] and the interface energy needed to create a ledge along the precipitate on the slip plane [8] have been suggested. Experimentally, efforts to illuminate the most important mechanisms have not produced data that support a clear consensus [9–13].

As computer resources become more accessible, atomistic simulations have continued to become a more viable tool for investigating these questions. While work has been done on dislocation–precipitate interactions (e.g. [14–17]), GP zones have not been studied. These studies point out that the dislocation–precipitate interactions can be very complex due to the variety of interacting phenomena, and may also involve changes in dislocation core structure and phase transformations. It is also reported that, while the precipitate strength can be predicted roughly using continuum theory, atomistic simulations are necessary to reveal the exact nature of the dominant mechanism. To be relevant, all simulations of this nature must use accurate

* Corresponding author. Tel.: +1 607 255 7155; fax: +1 607 255 9004.
E-mail address: dhw52@cornell.edu (D.H. Warner).

binary interatomic potentials and address the challenge associated with eliminating artificial boundary effects due to the long-range fields of dislocations.

Here we use atomistic simulations to examine dislocation–GP zone interactions. Focus is directed towards the technologically relevant class of Al–Cu alloys using a newly developed angular dependent Al–Cu potential. Long-range forces between the simulation cell boundaries and the dislocation are minimized via a brute force approach by using large simulation cells (we used approximately 600,000 CPU hours over the course of this study). Within the large parameter space of dislocation–GP zone interactions, attention is given to pure edge dislocations in the athermal limit. Screw dislocation interactions and the role of thermal activation are left as topics for future work. As a whole, this work fits into a larger effort to understand the age hardening process by providing input for continuum and discrete dislocation dynamics models [18]. Accordingly, the critical resolved shear stress at which the dislocation overcomes GP zones, τ_c , is a focal point.

2. Methodology

2.1. Interatomic interactions

The atomistic simulations were carried out using the freely available open source LAMMPS code [19]. The code was modified to use a recently developed Al–Cu empirical potential developed by Apostle and Mishin [20]. The potential is an angular dependent extension of the embedded atom method (EAM) [21,22], where the potential energy of the system is

$$E_{tot} = \frac{1}{2} \sum_{i,j(j \neq i)} \Phi_{ij}(r_{ij}) + \sum_i F_i(\bar{\rho}_i) + \frac{1}{2} \sum_{i,\alpha} (\mu_i^\alpha)^2 + \frac{1}{2} \sum_{i,\alpha,\beta} (\lambda_i^{\alpha\beta})^2 - \frac{1}{6} \sum_i v_i^2 \quad (1)$$

The indices i and j enumerate atoms and the superscripts α , $\beta = 1, 2, 3$ refer to the Cartesian directions. The first two terms, taken together, represent regular EAM contributions, where Φ_{ij} is the pair-interaction potential and F_i is the embedding energy of atom i with $\bar{\rho}_i$, which loosely represents the electron density. The three remaining terms represent the angular dependence through dipole and quadrupole distortions. The details of the potential can be found in Refs. [20,22]. We validated our implementation by comparing relaxed cohesive energies, vacancy formation energies, surfaces energies, heats of solution and formation energy for the θ' (Al₂Cu) phase with independent values provided by Apostle and Mishin [20].

2.2. Boundary conditions, geometry and loading

The simulation cell (Fig. 1a) consisted of a face-centered cubic Al lattice, bounded by $(\bar{1}10)$, (111) and $(11\bar{2})$ faces in the X , Y and Z directions, respectively. Periodic boundary

conditions were applied in the X and Z directions, whereas the Y surfaces were used to apply the load. Starting from a perfect lattice, a GP zone was created by simply changing selected atom types to Cu. The continuum displacement field of an edge dislocation was used to create a dislocation in the center of the simulation cell ($X = Y = 0$) with a line direction parallel to the Z -axis and $\vec{b} = 1/2[\bar{1}10]$.

There are three experimentally relevant orientations for edge dislocation–GP zone interactions. To examine these cases, we consider a constant dislocation orientation (as specified above) and two GP zone orientations: GP zones lying on the (100) and (001) planes (Fig. 1b). While GP zones also form on (010) planes, the dislocation interaction associated with this orientation is crystallographically equivalent to the (100) GP zone. The Burgers vector of the edge dislocation lies in the (001) GP zone plane, whereas it is offset by 60° from the (100) GP zone plane. From here on, we will refer to these GP zones by their misorientation with respect to the Burgers vector. As a simplification, we assume GP zones are monolayers of Cu atoms with a 100% Cu content. Experimental evidence suggests that the Cu content of GP zones may vary [23,24].

The minimum cell size was approximately $34 \times 42 \times 16$ nm³ and contained roughly 1.4 million atoms. For the simulations with particularly large GP zones (diameter > 6 nm) a larger cell size was used. In all cases, box size studies were performed to verify that simulation cell boundary forces were negligible in the X and Y directions. In the Z direction the size dependence was observed to follow the Orowan equation ($\tau_c \propto 1/L$), allowing extrapolation of the results obtained herein [25].

Prior to loading, NPT dynamics were performed for 50 ps to relax the system and alleviate out-of-balance forces and net stresses. The system was then loaded in shear by subjecting the atoms near the top and bottom Y surfaces to a constant traction in the X direction given by

$$f_{\text{top}} = \frac{\tau_{xy} A_{xz}}{N}, \quad f_{\text{bottom}} = -\frac{\tau_{xy} A_{xz}}{N} \quad (2)$$

for the top and bottom Y surfaces, respectively, where τ_{xy} is applied shear stress, A_{xz} is the surface area and N is the number of atoms on the respective surfaces. The applied shear stress was increased quasi-statically until the dislocation breaks free from the GP zone. At each load step of 5 MPa, a nonlinear conjugate gradient was performed to minimize the out-of-balance forces to less than 10^{-8} eV/Å.

In order to visualize the position and motion of the dislocation, we employ the “centro-symmetry parameter” [26] which represents a measure of the defective environment of the crystal. For this purpose, we use AtomEye visualization software [27].

3. Results

3.1. GP zone hardening and the effect of zone size

We begin our presentation of the results by simultaneously considering both GP zone orientations with a

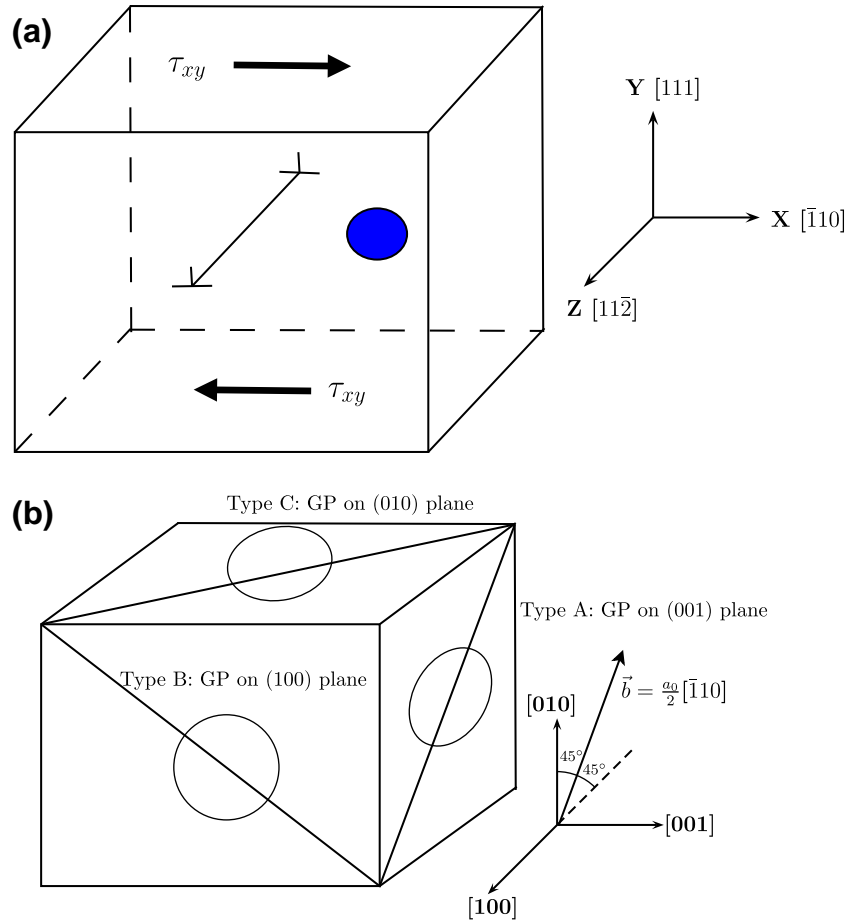


Fig. 1. (a) Simulation cell with edge dislocation and a GP zone; (b) three possible GP zone orientations with respect to Burgers vector. Types B and C are equivalent.

typical diameter of 4.4 nm [28–30,24]. In both cases the GP zone is positioned so that the slip plane of the dislocation intersects its center.

Before the application of the load, the system is relaxed via energy minimization. During this relaxation, the equilibrium misfit strain field due to the lattice mismatch forms. The relaxation also allows the full dislocation, which was created using a linear elastic analytic solution, to relax into two partial dislocations separated by a stacking fault spanning a distance of 1.0 nm. Upon relaxation, the leading partial of the dislocation is 3.6 nm from the edge of the 0° GP zone and 4.1 nm from the edge of the 60° GP zone. The fact that the dislocation does not glide during this relaxation suggests that the misfit stress and the elastic modulus mismatch forces acting on the dislocation are below the Peierls stress (≈ 3 MPa) at this distance. Upon application of the load, the leading partial glides up to the GP zone at an applied stress of 15 MPa ($0.026\tau_{Orowan}$) for the 0° zone and 30 MPa ($0.053\tau_{Orowan}$) for the 60° zone, where $\tau_{Orowan} = \frac{Gb}{L} = \frac{31.6 \text{ GPa} \times 2.86 \text{ \AA}}{158.7 \text{ \AA}} \approx 570$ MPa, representing the critical theoretical stress to induce Orowan looping [25]. Thus there appears to be a very mild repulsive interaction between the dislocation and the GP zones originating from the misfit stress field of the GP zone and possibly the mismatch in moduli.

As the load is increased, the edge dislocation does not shear the 0° GP zone but deposits itself along both surfaces of the GP zone plane. Thus the Cu atoms of the GP zone do not display a jump in displacements across the slip plane as the dislocation glides forward. This can be observed directly in Fig. 2 by examining the Cu atoms or indirectly by noticing that the centro-symmetry parameter indicates a different atomic structure on/near the GP zone plane after dislocation passing. While this mechanism is qualitatively similar to textbook Orowan looping [31], the stress measured for the dislocation to overcome the 0° GP zone in the simulation ($\tau_c = 185 \text{ MPa} = 0.32\tau_{Orowan}$) is much lower than the Orowan case due to the thin coherent nature of the GP zone allowing strong interaction with the opposite-signed dislocation looping segments.

For the 60° GP zone, where the Burgers vector of the dislocation can create a step in the GP zone plane, the interaction is different. As loading increases, the leading partial dislocation is observed to cut the GP zone, leaving a clear $b/2$ displacement jump across the Cu atoms (Fig. 3). After the leading partial cuts, the trailing partial remains pinned by the GP zone until the applied stress reaches 240 MPa or $0.42\tau_{Orowan}$. At this stress the trailing partial travels around the GP zone from one side, leaving a trailing partial loop. The formation of a trailing partial loop as the

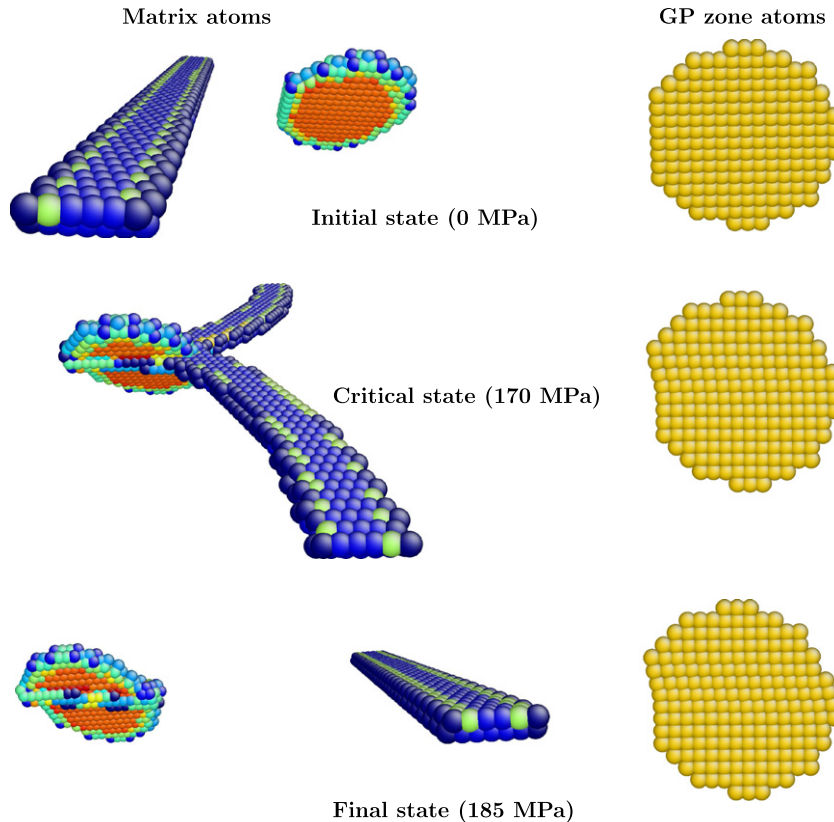


Fig. 2. Snapshots showing the dislocation interaction with a 4.4 nm 0° GP zone. The left column shows matrix (Al) atoms with a high centro-symmetry parameter. The right column shows only the Cu atoms of the GP zone. Note that after the dislocation overcomes the GP zone the Cu atoms do not show a displacement step and the centro-symmetry parameter reveals debris left along the face of the GP zone indicative of the dislocation looping around the GP zone.

critical mechanism controlling τ_c invalidates chemical arguments for this case as well.

For both GP zone orientations, the effect of GP zone size on τ_c was examined (Fig. 4).¹ In both cases, τ_c becomes independent of the zone size for large GP zones. For the 0° GP zone, the size independence follows from the full dislocation looping mechanism, i.e. for the dislocation to overcome the 0° GP zone the resolved shear stress must be great enough so that the dislocation deposits itself along the faces of the GP zone. However, for the 60° GP zone τ_c does not become size independent until larger sizes (≥ 8 nm). As with the 0° GP zone, the size independence of the 60° GP zone at large sizes likely results from dislocation looping being the controlling mechanism. At intermediate sizes (3–6 nm), the size dependence of 60° GP zone may be due to the $1/r$ interaction between the trailing partial dislocation segments on each side of the GP zone, the forces of which would favor the looping process more as the GP zone size decreases. For small 60° GP zone sizes (< 3 nm),

the mechanism changes and full cutting is observed, i.e. the top and bottom GP zone planes separate by a full Burgers vector after dislocation passes the GP zone. Thus, the size dependence in this smaller region would be expected to be linear, following the chemical energy associated with simple GP zone ledge creation models [32].

3.2. Effect of GP zone offset

In order to simplify analysis and limit computational expense, many analytic and/or computational models assume that the dislocation glide plane only intersects the precipitate through its center. However, in reality dislocations intersect precipitates at all locations or “offsets”. For GP zones we find that the offset between the glide plane and precipitate center is a significant parameter controlling not only τ_c , but the mechanism by which the dislocation overcomes the precipitate. Fig. 5a depicts how we have quantified offset in normalized units from -8 to $+8$ for both orientations of a GP zone with a 4.4 nm diameter. Each unit represents the atomic spacing in the $[1\ 1\ 1]$ direction; $o = a_0/\sqrt{3}$, where a_0 is the lattice constant. As can be seen in Fig. 5b, τ_c does not scale with the dislocation–GP zone intersection surface area, contrary to textbook precipitate cutting models [31]. In general, τ_c increases as the extra plane of atoms associated with the edge dislocation

¹ In Fig. 4, GP zone diameters greater than 6 nm required an increased simulation box size in the Z direction to avoid boundary effects. Therefore, to be consistent, the stresses reported in Fig. 4 are rescaled to correspond to the same box size as the simulations conducted with the standard box size of $34 \times 42 \times 16$ nm³, as given in the Methodology section.

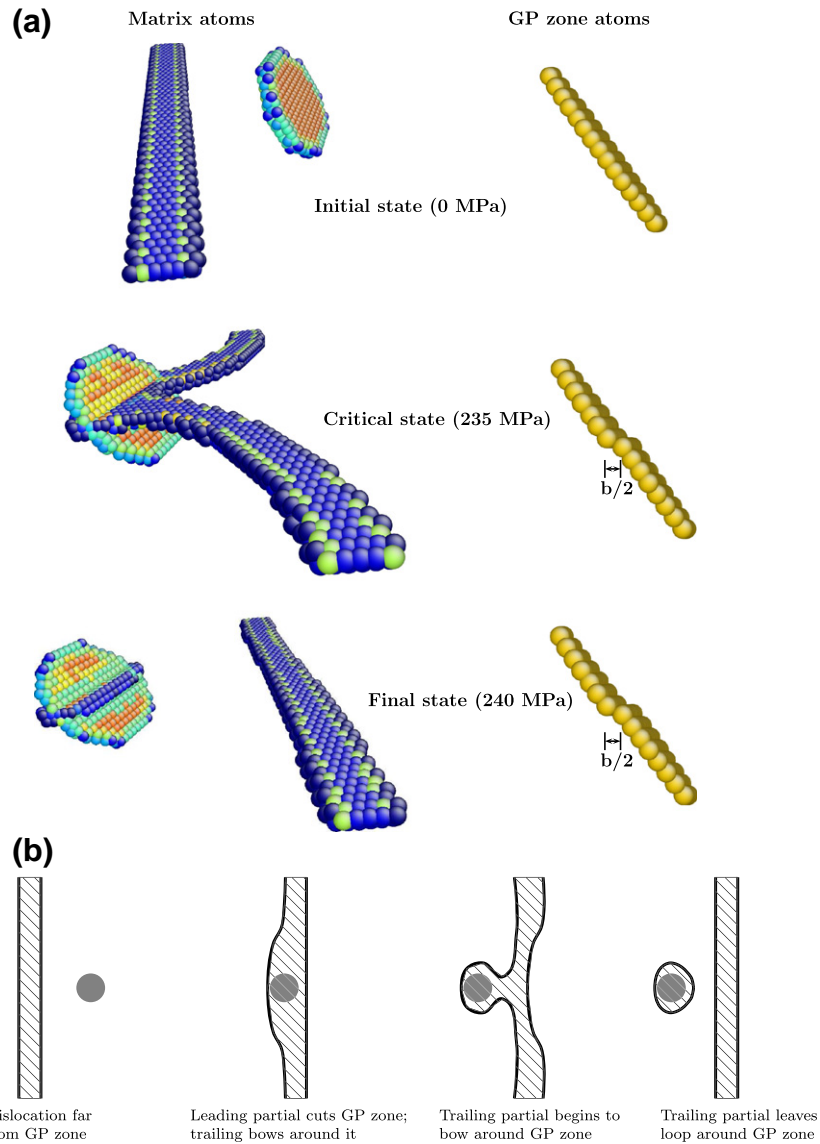


Fig. 3. Snapshots showing the dislocation interaction with a 4.4 nm 60° GP zone. (a) The left column shows matrix (Al) atoms with a high centrosymmetry parameter and the right column shows Cu atoms inside the GP zone. Note that after the dislocation overcomes the GP zone the Cu atoms are only displaced by half a Burgers vector and the centro-symmetry parameter reveals a defect structure around the GP zone indicative of the partial dislocation loop. (b) Cartoon illustrating the process of leading partial cutting with trailing partial looping.

interacts with more of the GP zone (which is denoted here by a more positive offset). This is in accordance with the interaction of the dislocation and GP zone hydrostatic stress fields, i.e. the stress field generated by the extra plane of atoms associated with the edge dislocation interacts with the lattice misfit stress field associated with the GP zone.

For the 0° orientation, all offsets < 2 display the mechanism given in the previous section, i.e. full dislocation looping. Over this range, the effect of offset on τ_c is very close to linear, with a slope of $0.015\tau_{Orowan}$ per unit offset with $R^2 = 0.98$ (Fig. 5b). For offsets ≥ 3 with the 0° orientation, a defect structure is nucleated at the intersection of the dislocation and the GP zone and travels along the dislocation line, making the dislocation sessile (Fig. 6). The defect results from the rearrangement of aluminum atoms border-

ing the GP zone. Copper atoms are not directly involved in the process. To better investigate the relevance of this process, i.e. examine whether it is a 0 K artifact, an additional simulation was performed at 77 K. At 77 K, the same defect structure did nucleate at the intersection between the dislocation and GP zone but did not propagate along the dislocation line as it did at 0 K. At 77 K, the dislocation overcame the GP zone in the same manner as described for low offsets at 0 K. Thus, the defect nucleation mechanism observed here may not be relevant to experiments at finite temperature.

For the 60° GP zone, the same defect nucleation mechanism is observed, making the dislocation sessile at offsets of 4–6. At an offset of 7, where the slip plane intersects the GP zone such that dislocation slip would only displace a

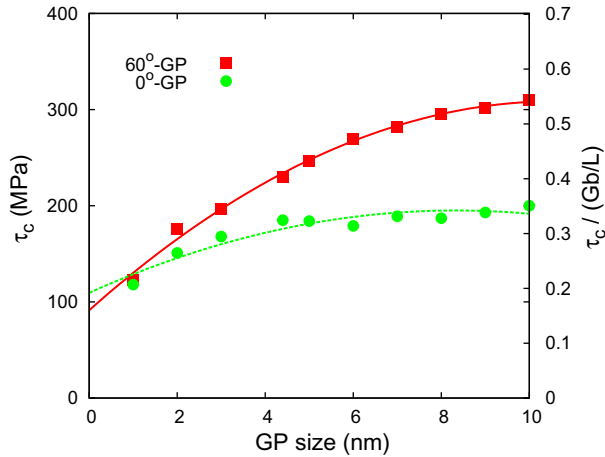


Fig. 4. The shear stress required for a dislocation to overcome the GP zone vs. its diameter. The lines serve as guides for the eye.

single row of Cu atoms if cutting were to occur, a different mechanism occurs. The segment of the dislocation that

directly interacts with the Cu atoms of the GP zone climbs up one plane and thus avoids direct interaction with the GP zone (Fig. 7). For the dislocation segment to climb, the Al atoms bordering the top of the GP zone must become part of the dislocation, thus creating a row of vacancies along the top of the GP zone after the dislocation passes. We note that 0 K diffusionless climb processes have also been reported by Osetsky and Bacon [14] for impenetrable Cu obstacles in body-centered cubic α -Fe. As with the defect structure nucleated at lesser offsets, we reran the simulation at $T = 77$ K to examine the feasibility of the mechanism at finite temperature. At 77 K, the same climbing mechanism is observed.

For the 60° GP zone at offsets less than 4, an approximately linear relation between τ_c and the offset is observed, with $0.012\tau_{Orowan}$ per unit offset and $R^2 = 0.90$ (Fig. 5b) if we exclude the pinning case at $o = -8$. Leading partial cutting with trailing partial looping is observed for offsets in the range $-4 < o < 4$, while full dislocation cutting is observed for offsets ≤ -4 . This is consistent with zero-offset

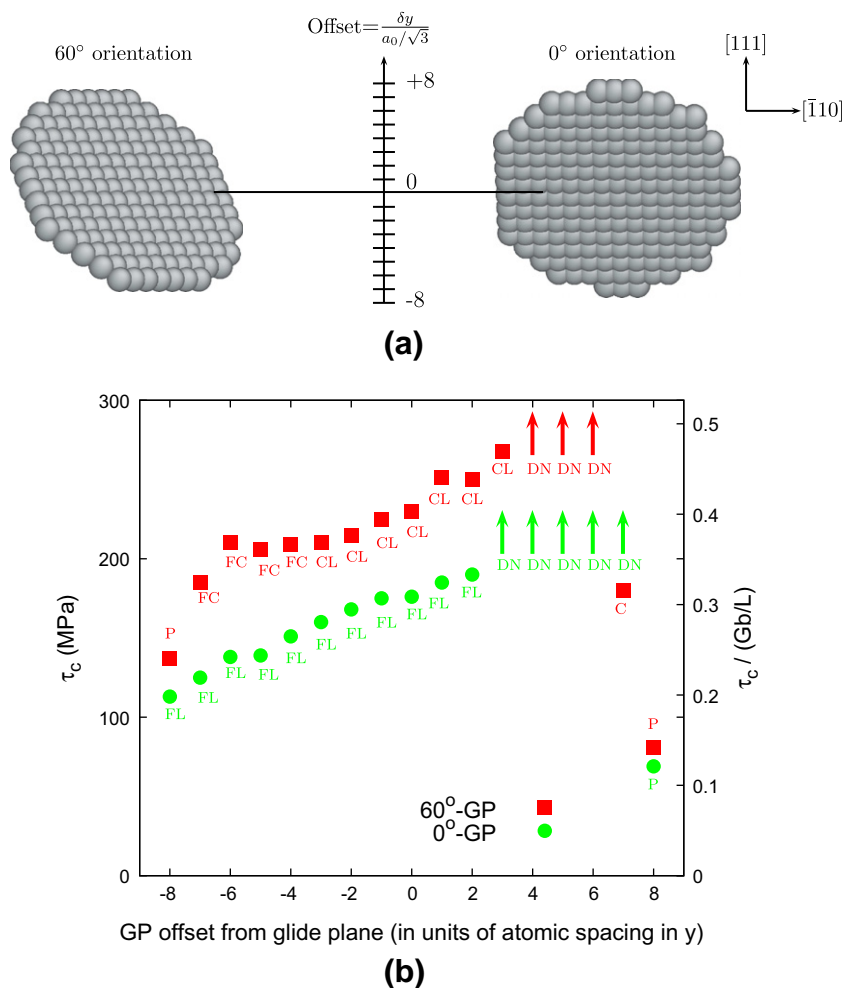


Fig. 5. Effect of GP offset with respect to dislocation glide plane. (a) Location of the dislocation glide plane with respect to the GP zone; (b) the variation of stress required for the dislocation to overcome the GP zone as a function of offset. In (b), text abbreviations are used to represent specific mechanisms: FC = full dislocation cutting; CL = leading partial cutting with trailing dislocation looping; FL = full dislocation looping; P = pinning; DN = defect nucleation; C = climb. Arrows mean $\tau_c > 400$ MPa.

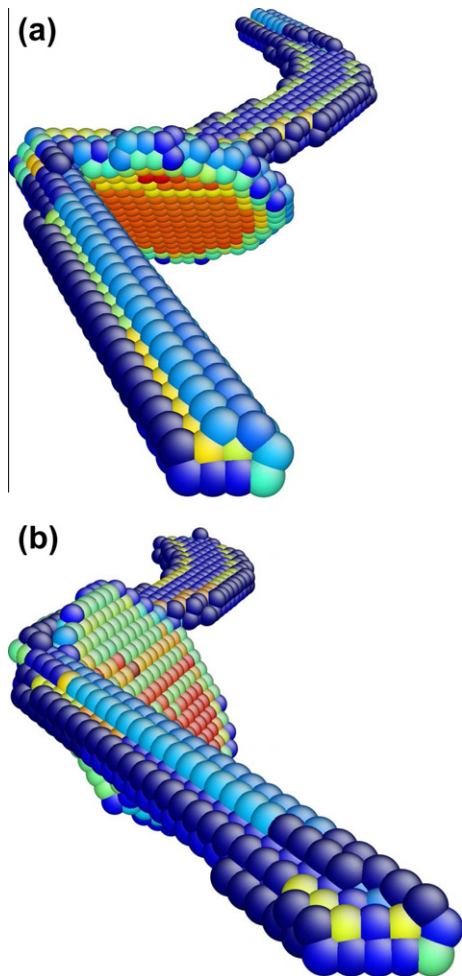


Fig. 6. Defect nucleation and propagation along the line of the dislocation, making it sessile (offset = +4): (a) 0° GP zone; (b) 60° GP zone.

results for different GP sizes, with full cutting being observed at small GP zone sizes and partial cutting and looping being observed for larger ones.

Finally, as a reference, in Fig. 5b we report several stresses for which the dislocation glide plane intersects the edge of the GP zone, i.e. the plane which has Cu on one side and Al on the other. In Fig. 5b these values are referenced as pinning similar to a dislocation being pinned by a solute atom. Note that in all cases pinning provides appreciable hardening.

3.3. Multiple cutting

Another simplification common to precipitate hardening studies is to limit focus to the interaction of a precipitate with a single dislocation. However, precipitates are likely to interact with multiple dislocations even before macroscopic yielding ensues. We have attempted to investigate this effect for both GP zone orientations. The GP zone diameters were taken as 4.4 nm and the slip plane was chosen to intersect GP zones through their centers. The simulations were conducted using the same simulation

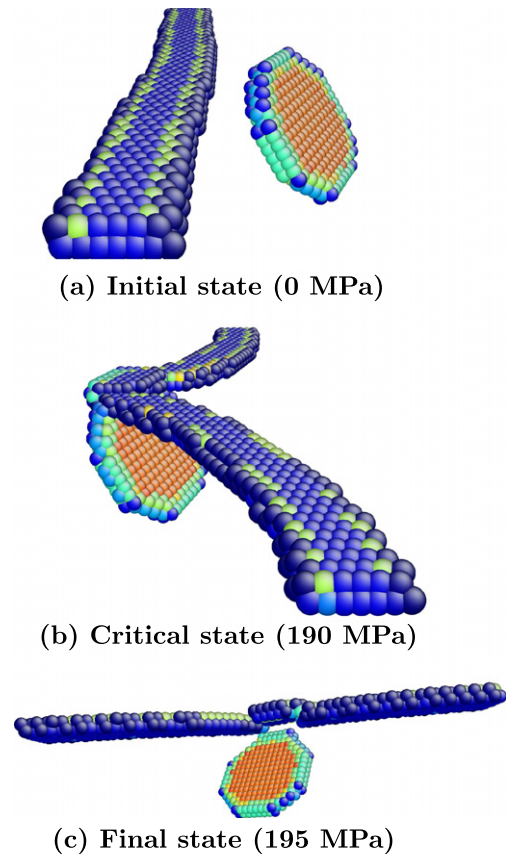


Fig. 7. Diffusionless climb mechanism for 60° GP zone at high offset (offset = +7): (a) initial state; (b) critical state; (c) final state.

set-up as the previous studies with the exception that the load was applied using displacement boundary conditions.² By using displacement boundary conditions, the load drops substantially after the dislocation overcomes the GP zone. After overcoming the GP zone, the dislocation traverses the simulation cell and crosses the periodic boundary, coming to rest when it reaches the GP zone for the second time. Then, as the applied displacements are again increased, the dislocation will overcome the GP zone for a second time. Thus, the simulations allow τ_c to be recorded for multiple passes of dislocations through GP zones (Fig. 8).

The two orientations of GP zones give markedly different responses for multiple dislocation interactions, in line with the differences in underlying mechanisms. For the 0° GP zone, τ_c increases for the second dislocation interaction due to the dislocation loop that is left behind by the first. For the third dislocation, a defect structure is nucleated at the GP zone which propagates along the dislocation line, making it sessile, as was observed for high offsets in the case of single cutting.

For the 60° GP zone, the first dislocation overcomes it by the leading partial cutting the zone and the trailing

² Displacement boundary conditions with our simulation cell size can produce an error of ≈ 10 MPa in τ_c relative to the more accurate values obtained in the previous sections using applied force boundary conditions.

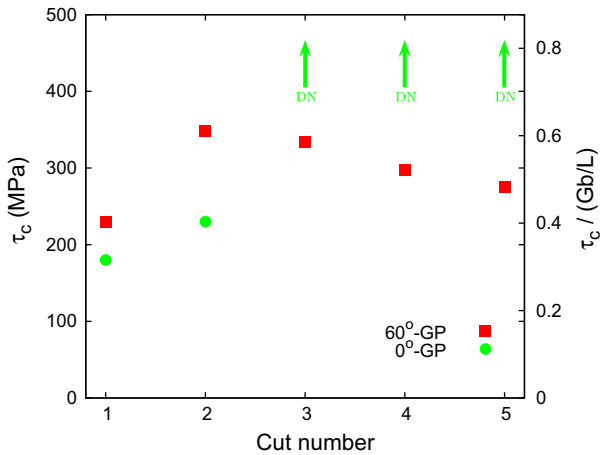


Fig. 8. Multiple dislocation interactions with 4.4 nm GP zones at 0 K. Arrows mean $\tau_c > 500$ MPa due to defect nucleation.

partial creating a partial dislocation loop. When the second dislocation comes into contact with the GP zone, the partial loop left behind from the first dislocation collapses, increasing the displacement jump at the GP zone to a full Burgers vector. The second dislocation overcomes the GP zone in a full Orowan looping fashion; however, the leading partial component of the full loop collapses, leaving a trailing partial loop at the GP zone. The third, fourth and fifth dislocations overcome the GP zone in the same way as the second. As the two halves of the GP zone separate with successive cuts, τ_c decreases for all the cuts after the second.

4. Discussion

A tenet of traditional physical metallurgy is that small precipitates are cut by dislocations while larger ones are not [31,33]. This concept, along with precipitate growth kinetics, is key to the existence of a maximum in the hardness vs. aging time relations. In simple models, peak hardness is often associated with the aging time during which the precipitates change from being shearable to being impenetrable [31]. Thus, considering that GP zones form well before peak aging and have a coherent nanometer sized structure, it is natural to infer that they are shearable precipitates [31,32].

Surprisingly, in this study, GP zone cutting is not a widely observed mechanism as it is only found to be the controlling mechanism for a small subset of all configurations studied, i.e. 60° GP zones with diameters <3 nm. For the significant majority of cases studied here, dislocation looping is the controlling mechanism (considering both full dislocation looping and leading partial cutting with trailing partial looping). The resolved stress at which looping occurs is significantly below the continuum Orowan prediction [32]. This difference is likely due to the coherent and atomically thin nature of the GP zones, which permits strong dislocation segment interaction forces. The general proclivity for dislocation looping as opposed to

cutting may be due to the absence of thermal activation in our simulations. This is currently an area that we are investigating thoroughly within a transition state framework.

Dislocation looping around GP zones naturally leads to a τ_c that is independent of GP zone size for large diameters in both orientations. Interestingly, the same trend would also exist if the dominant mechanism was GP zone cutting, controlled by the ledge creation energy. The 0° GP zone, being coplanar with the Burgers vector, requires the same area of ledge regardless of GP zone size, suggesting a τ_c that is size independent. On the other hand, the 60° GP zone requires a ledge size proportional to the GP zone size; nevertheless, it is likely that this ledge is not created uniformly, but rather by the dislocation zipping across the face of the GP zone. This would give a τ_c that is only dependent on the energy required to create the initial segment of ledge. Thus, a maximum τ_c exists for GP zones regardless of whether the mechanism is cutting or looping. This is consistent with the aging curves, which show a plateau in the hardness near the end of GP zone strengthening (note that aging kinetics may also be the cause of this plateau) [29].

While looping is by far the most common mechanism controlling τ_c , a number of other mechanisms were observed. The size of the GP zone, its orientation relative to the dislocation, the location where the dislocation and the GP zone intersect, and the number of dislocations that have previously passed on the slip plane are all controlling factors. Full dislocation looping, leading partial cutting with trailing partial looping, dislocation cutting, 0 K climb via the nucleation of vacancies and the formation of a defect structure making the dislocation sessile are all mechanisms that were observed. The formation of a sessile dislocation appears to be an artifact of lack of thermal activation in our simulations as it was not observed at 77 K. However, diffusionless climb did occur at 77 K and would likely be a viable mechanism under experimental conditions. Leading partial cutting with trailing partial looping is a mechanism that has not been reported in the literature; however, its existence seems completely plausible.

A primary goal of this work was to obtain τ_c for dislocation–GP zone interactions, with the motivation being that τ_c provides a basis for comparison with other dislocation–precipitate interactions relevant to the age-hardening process (something which we intend to study in forthcoming works). However, we have found that it is hard to associate τ_c with a single value as it depends significantly on the GP zone dislocation interaction parameter space. As a first approximation one might ignore the effects of multiple cutting, and leave out the sessile dislocation formation and climb mechanisms. Under these assumptions, τ_c at zero offset can be considered the average value for a dislocation to overcome a GP zone of a certain size, using the observation that τ_c is approximately linear with offset.

Considering GP zones with 5 nm diameters and a spacing of 8 nm, a Taylor factor of three predicts yield strengths of

approximately 1200 MPa using the values obtained in these simulations and the Orowan equation. Experimentally, yield strengths of 100–400 MPa are typical for underaged Al–Cu alloys, the precipitates of which are thought to be primarily GP zones [34,13]. This large overprediction of strength should not be a surprise considering the athermal nature of our simulations. Additionally, a more careful mapping between the stress needed for a dislocation to overcome a single GP zone and the shear stress required to create plastic flow in a single crystal would likely yield lower strengths [35]. The effect of dislocation character must also be considered when relating these results to material flow strength. Our preliminary simulations of screw dislocation–GP zone interactions show that the cross-slip mechanism is highly active even at the athermal limit. This suggests that GP zones are less of an impediment to screw dislocation motion and thus screw dislocations likely play less of a role in determining precipitate-hardened flow strengths.

5. Conclusions

In summary, we have studied the athermal interactions of edge dislocations with GP zones in Al–Cu alloys using a recently developed Al–Cu interatomic potential. A significant complexity surrounding these interactions is revealed as edge dislocations are found to overcome GP zones by several mechanisms, depending upon the GP zone size, orientation and offset with respect to the dislocation glide plane. In contrast to many classical models, we observe dislocation looping to be the controlling mechanism by which dislocations overcome GP zones in the majority of cases. Thus, models based on ledge creation are not consistent with our observations, at least in the athermal limit. When the GP zone plane does not coincide with the Burgers vector of the dislocation, a new mechanism has been identified where the leading partial cuts the GP zone and the trailing partial loops around it. Diffusionless dislocation climb has also been observed when the dislocation intersects the edge of the GP zone. Contrary to some models, elastic interactions do not significantly affect dislocation motion when the dislocation is not in contact with the GP zone. When GP zones are small, their size influences the critical resolved shear stress for a dislocation to overcome them. However, as they become larger, a maximum strength is reached, limiting GP zone strengthening. In the athermal limit, the maximum is found to be about $0.35\tau_{Orowan}$ for a GP zone with 0° misorientation, and $0.55\tau_{Orowan}$ for 60° misorientation.

Acknowledgements

The authors gratefully acknowledge support from Ed Glaessgen and Steve Smith at NASA (Grant No. NNX08BA39A).

References

- [1] Guinier A. *Ann Phys* 1939;12:161.
- [2] Preston GD. *Philos Mag* 1938;26:855.
- [3] Mott NF, Nabarro FRN. In: Report of a conference on strength of solids. London: The Physical Society; 1948. p. 1.
- [4] Gerold V, Haberkorn H. *Phys Status Solidi* 1966;16:675.
- [5] Knowles G, Kelly PM. In: BSC/ISI conference, Scarborough. London: The Iron and Steel Institute; 1971. p. 9.
- [6] Nembach E. *Phys Status Solidi (a)* 1983;78:571.
- [7] Hirsch PB, Kelly A. *Philos Mag* 1965;12:881.
- [8] Kelly A. In: Electron microscopy and strength of crystals. London: John Wiley and Sons; 1963. p. 947.
- [9] Kelly A, Fine ME. *Acta Metall* 1957;5:365.
- [10] Harkness SD, Hren JJ. *Met Trans* 1970;1:43.
- [11] Brown LM, Ham RK. In: Strengthening methods in crystals. London: Applied Science Publishers; 1971. p. 9.
- [12] Eto T. *Scripta Metall* 1980;14:133.
- [13] Muraishi S, Niwa N, Maekawa A, Kumai S, Sato A. *Philos Mag A* 2002;82:2755.
- [14] Osetsky YN, Bacon DJ. *J Nucl Mater* 2003;323:268.
- [15] Chen Z, Kiousis N, Ghoniem N. *Phys Rev B* 2009;80:184104.
- [16] Shim JH, Cho YW, Kwon SC, Kim WW, Wirth BD. *Appl Phys Lett* 2007;90:021906.
- [17] Terentyev D, Bonny G, Malerba L. *Acta Mater* 2008;3229.
- [18] van der Giessen E, Needleman A. *Model Simul Mater Sci* 1995;3:689.
- [19] Plimpton SJ. *J Compos Phys* 1995;117:1.
- [20] Apostle F, Mishin Y; unpublished.
- [21] Daw MS, Baskes MI. *Phys Rev B* 1984;29:6443.
- [22] Mishin Y, Mehl M, Papaconstantopoulos D. *Acta Mater* 2005;53:4029.
- [23] Hono K, Satoh T, Hirano KI. *Philos Mag A* 1986;53:495.
- [24] Karlik M, Bigot A, Jouffrey B, Auger P, Belliot S. *Ultramicroscopy* 2004;98:219.
- [25] Orowan E. In: Symposium on internal stresses in metals and alloys. London: Institute of Metals; 1948. p. 451.
- [26] Kelchner C, Plimpton S, Hamilton J. *Phys Rev B* 1998;58:11085.
- [27] Li J. *Model Simul Mater Sci* 2003;11:173.
- [28] Karlik M, Jouffrey B. *Acta Mater* 1997;45:3251.
- [29] Ringer SP, Hono K. *Mater Charact* 2000;44:101.
- [30] Konno TJ, Hiraga K, Kawasaki M. *Scripta Mater* 2001;44:2303.
- [31] Hull D, Bacon D. *Introduction to dislocations*. 4th ed. Woburn (MA): Butterworth; 2001.
- [32] Martin JW. *Precipitation hardening*. 2nd ed. Woburn (MA): Butterworth; 1998.
- [33] Dieter GE. *Mechanical metallurgy*. 3rd ed. New York: McGraw-Hill; 1986.
- [34] Silcock JM, Heal TJ, Hardy HK. *J Inst Met* 1953–54;82:239.
- [35] Chakravarty SS, Curtin W. *J Mech Phys Solids* 2010;58:625.